

# Mixed-Domain Fast Simulation of RF and Microwave MEMS-based Complex Networks within Standard IC Development Frameworks

Jacopo Iannacci

*Fondazione Bruno Kessler – FBK, MemSRaD Research Unit  
Italy*

## 1. Introduction

MEMS technology (MicroElectroMechanical-System) has been successfully employed since a few decades in the sensors/actuators field. Several products available on the market nowadays include MEMS-based accelerometers and gyroscopes, pressure sensors and micro-mirrors matrices. Beside such well-established exploitation of MEMS technology, its use within RF (Radio Frequency) blocks and systems/sub-systems has been attracting, in recent years, the interest of the Scientific Community for the significant RF performances boosting that MEMS devices can enable. Several significant demonstrators of entirely MEMS-based lumped components, like variable capacitors (Hyung et al., 2008), inductors (Zine-El-Abidine et al., 2003) and micro-switches (Goldsmith et al., 1998), are reported in literature, exhibiting remarkable performance in terms of large tuning-range, very high Q-Factor and low-loss, if compared with the currently used components implemented in standard semiconductor technology (Etxeberria & Gracia, 2007, Rebeiz & Muldavin, 1999). Starting from the just mentioned basic lumped components, it is possible to synthesize entire functional sub-blocks for RF applications in MEMS technology. Also in this case, highly significant demonstrators are reported and discussed in literature concerning, for example, tuneable phase shifters (Topalli et al., 2008), switching matrices (Daneshmand & Mansour, 2007), reconfigurable impedance matching networks (Larcher et al., 2009) and power attenuators (Iannacci et al., 2009, a). In all the just listed cases, the good characteristics of RF-MEMS devices lead, on one side, to very high-performance networks and, on the other hand, to enabling a large reconfigurability of the entire RF/Microwave systems employing MEMS sub-blocks. In particular, the latter feature addresses two important points, namely, the reduction of hardware redundancy, being for instance the same Power Amplifier within a mobile phone suitable both in transmission (Tx) and reception (Rx) (De Los Santos, 2002), and the usability of the same RF apparatus in compliance with different communication standards (like GSM, UMTS, WLAN and so on) (Varadan, 2003). Beside the exploitation of MEMS technology within RF transceivers, other potentially successful uses of Microsystems are in the Microwave field, concerning, e.g., very compact switching units, especially appealing to satellite applications for the very reduced weight (Chung et al., 2007), and phase shifters in order to electronically steer short

and mid-range radar systems for the homeland security and monitoring applications (Maciel et al., 2007).

Given all the examples reported above, it is straightforward that the employment of a proper strategy in aiming at the RF-MEMS devices/networks optimum design is a key-issue in order to gain the best benefits, in terms of performance, that such technology enables to address. This is not an easy task as the behaviour of RF-MEMS transversally crosses different physical domains, namely, electrical, mechanical and electromagnetic, leading to a large number of trade-offs between mechanical and electrical/electromagnetic parameters, that typically cannot be managed within a unique commercial simulation tool.

In this chapter, a complete approach for the fast simulation of single RF-MEMS devices as well as of complex networks is presented and discussed in details. The proposed method is based on a MEMS compact model library, previously developed by the author, within a commercial simulation environment for ICs (integrated circuits). Such software tool describes the electromechanical mixed-domain behaviour typical of MEMS devices. Moreover, through the chapter, the electromagnetic characteristics of RF-MEMS will be also addressed by means of extracted lumped element networks, enabling the whole electromechanical and electromagnetic design optimization of the RF-MEMS device or network of interest. In particular, significant examples about how to account for the possible non-idealities due to the employed technology as well as for post-processing steps, like the encapsulation of the MEMS within a package, will be reported. The optimization methodology, along with practical hints reported in this chapter, will help the RF-MEMS designer in the fast and proficient reaching of the optimum implementation that maximizes the performance of the device/network he wants to realize within a certain technology.

## 2. MEMS Compact Model Software Library

The MEMS compact model library adopted in the next pages, for the simulation of RF-MEMS devices and networks, has been previously developed by the author within the Cadence™ IC framework by using the VerilogA® HDL-based (hardware description language) syntax (Jing et al., 2002). The library features basic components, that are described by suitable mathematical models, and that connect with the surrounding elements by means of a reduced number of nodes. This enables the composition of complex MEMS devices geometries at schematic-level, as it is usually done when dealing with standard electronic circuits. The most important components available in the library are the rigid plate electrostatic transducers (realizing suspended air-gaps) and the flexible straight beam defining the elastic suspensions. Beside such main elements, the library also includes anchoring points and mechanical stimuli (like forces and displacements) in order to apply the proper boundary conditions to the analyzed MEMS structure schematic. The air-gap and flexible beam models are described more in details in the following two subsections.

### 2.1 Suspended Rigid Plate Electromechanical Transducer

Being this element a rigid body, the mechanical model is rather simple as it is based on the forces/torques balancing between the four plate vertexes, where the nodes are placed and where the plate is connected to other elements, and the centre of mass (Fedder, 2003). The model includes 6 DOFs (degrees of freedom) at each vertex, namely, 3 linear displacements and 3 rotation angles around the axes. Fig. 1 shows the schematic of the rigid plate in a

generic position in space where all the DOFs are highlighted for each of the 4 vertexes labelled as NW, NE, SE and SW (North-West, North-East, South-East and South-West, respectively). The forces/torques applied to each node are transferred and summed into the centre of mass (CM in Fig. 1) according to the well-known equation of dynamics:

$$F = mA \tag{1}$$

where  $F$  is the applied force,  $m$  the mass of the plate and  $A$  its acceleration in a certain direction. The force/torque contributions are summed separately depending on the DOF/DOFs involved.

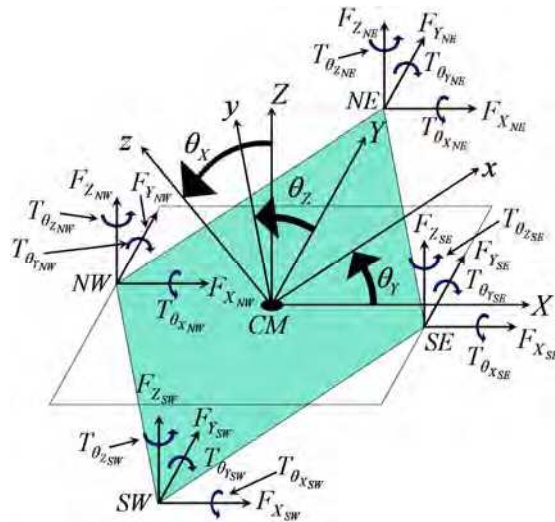


Fig. 1. Schematic of the rigid suspended plate in a generic position with all the 24 DOFs highlighted (6 DOFs per each vertex, namely, 3 linear DOFs and 3 rotational DOFs).

The rigid plate element also includes a contact model that manages the collapse onto the underneath electrode (pull-in) and the transduction between the electrical and mechanical domain, accounting for the capacitance and the electrostatic attractive force, between the suspended plate and the underneath electrode, when a biasing voltage is applied to them. Such magnitudes are calculated starting from well-known basic formulae, used in electrostatics, that have been extended to a double integral closed form, accounting for the most generic cases, when the plate assumes non-parallel positions with respect to the substrate. Given this consideration, the capacitance and electrostatic force are expressed as follows:

$$C = \frac{\epsilon}{\sigma} \int_{\frac{w}{2}}^{\frac{w}{2}} \int_{\frac{l}{2}}^{\frac{l}{2}} \frac{dxdy}{Z(x, y, \theta_x, \theta_y, \theta_z)} \tag{2}$$

$$F = \frac{1}{2} \frac{\epsilon V^2}{\sigma^2} \int_{-\frac{W}{2}}^{\frac{W}{2}} \int_{-\frac{L}{2}}^{\frac{L}{2}} \frac{dxdy}{Z(x, y, \theta_x, \theta_y, \theta_z)^2} \quad (3)$$

where  $\epsilon$  is the permittivity of air,  $W$  and  $L$  are the plate dimensions,  $V$  is the voltage applied between the two plates and  $\sigma$  is a coefficient that accounts for the curvature of the electric field lines, occurring when the plate is tilted (i.e. non-parallel to the substrate). Note that the punctual distance  $Z$  between the suspended plate and the underlying electrode depends on the coordinates of each point integrated over the plate area and on the three rotation angles  $\theta_x$ ,  $\theta_y$  and  $\theta_z$ . The electrostatic transduction model also accounts for the effects due to the presence of holes on the plate surface, needed in order to ease the sacrificial layer removal, and to the fringing effects due to the distortion of the electric field lines in the vicinity of plate and holes edges. Finally, the description of the plate dynamics is completed by a model accounting for the viscous damping effect due to the air friction. Such model is based on the squeeze-film damping theory, and takes into account the presence of holes on the plate area. All the just listed rigid plate model features are not described here but are available in details in (Iannacci, 2007), together with their validation against FEM (Finite Element Method) simulated results and experimental data.

## 2.2 Flexible Straight Suspending Beam

The flexible straight beam model is based on the theory of elasticity (Przemieniecki, 1968) and the deformable suspension is characterized by two nodes, one per each end, including 6 DOFs, 3 linear and 3 angular deformations (or torques). Consequently, the beam has totally 12 DOFs as the schematic in Fig. 2 shows, and the whole static and dynamic behaviour is expressed by the following constitutive equation:

$$\mathbf{F} = \mathbf{K}\mathbf{X} + \mathbf{C}\dot{\mathbf{X}} + \mathbf{M}\ddot{\mathbf{X}} \quad (4)$$

where  $\mathbf{F}$  is the 12x1 vector of forces/torques corresponding to the 12 DOFs reported in Fig. 2,  $\mathbf{K}$  is the Stiffness Matrix, describing the elastic behaviour of each DOF,  $\mathbf{M}$  is the Mass Matrix, accounting for the inertial behaviour of each DOF and  $\mathbf{C}$  is the Damping Matrix, modelling the viscous damping effect. Moreover, it must be noticed that  $\mathbf{K}$ ,  $\mathbf{C}$ , and  $\mathbf{M}$  are multiplied by the 12x1 vector of linear/angular displacements  $\mathbf{X}$ , and by its first and second time derivatives, respectively, being the latter two the vectors of velocity and acceleration. It is straightforward that (4) is a generalization of (1) accounting for the whole behaviour of the flexible beam. The  $\mathbf{C}$  matrix is obtained by applying the same squeeze-film damping model adopted in the rigid plate. Finally, the beam model is completed by the electromechanical transduction model that accounts for the capacitance and electrostatic attractive force between the suspended deformable beam and the substrate. It is similar to the one reported in Subsection 2.1, even though it has been modified in order to account for the deformability of the beam. More details about the beam model and its validation are available in (Iannacci, 2007).

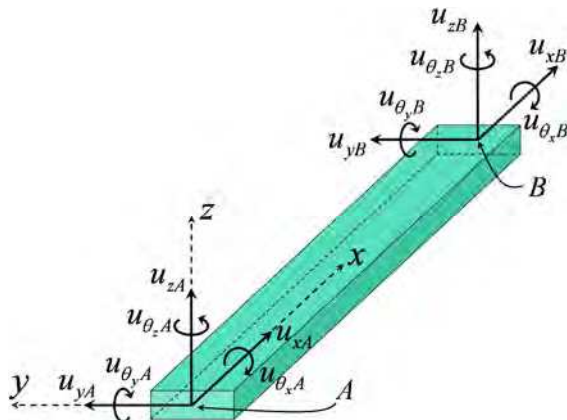


Fig. 2. Schematic of the 12 DOFs flexible straight beam. The 6 DOFs (3 linear and 3 angular) at each of the ends *A* and *B* are visible.

### 3. RF Modelling of a MEMS-based Variable Capacitor

In this section the complete modelling approach involving the RF and electromechanical behaviour of MEMS devices is introduced and discussed. A lumped element network describing the intrinsic RF-MEMS device and all the surrounding parasitic effects will be extracted from S-parameter measured datasets. Moreover, the MEMS device mechanical properties and electromechanical experimental characteristics will be exploited in order to prove the correctness of the RF modelling previously performed.

The specific analyzed RF-MEMS device is a variable capacitor (varactor) manufactured in the FBK RF-MEMS surface micromachining technology (Iannacci et al., 2009, a). An experimental 3D view obtained by means of an optical profiling system is reported in Fig. 3.

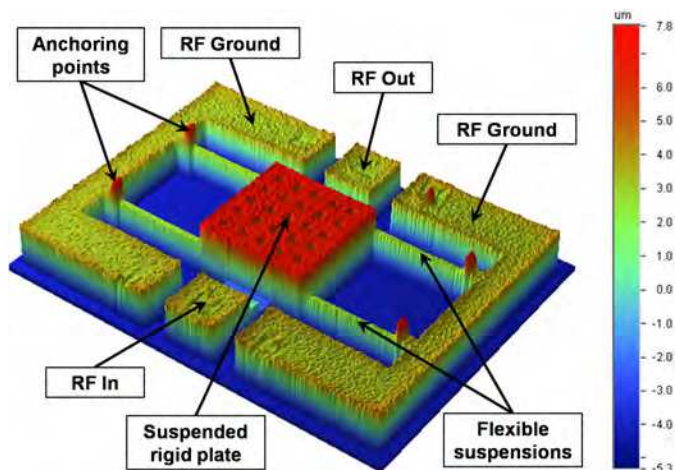


Fig. 3. 3D view of the studied RF-MEMS varactor obtained by means of an optical profiling system. The colour scale represents the vertical height of the sample.

The variable capacitance that loads the RF line (shunt-to-ground) is realized by a gold plate kept suspended over the underneath fixed electrode by four flexible straight beams. Depending on the DC bias applied between the two plates, the gold one gets closer to the substrate because of the electrostatic attraction, eventually collapsing onto it when the pull-in is reached, thus leading to the maximum capacitance value.

### 3.1 Equivalent Lumped Element Network Extraction

The lumped element network extraction, that is going to be discussed, starts from measured S-parameter datasets (2 ports) collected, on the same sample of Fig. 3, onto a probe station with GSG (ground-signal-ground) probes and an HP 8719C VNA (vector network analyzer) in the frequency range 200 MHz - 13.5 GHz. The controlling DC voltage that biases the suspended MEMS plate is applied directly to the RF probes by means of two bias-Tees. The DUT (device under test) is biased at different (constant) voltage levels. The performed VNA calibration is a SOLT (short, open, load, thru) (Pozar, 2004) on a commercial impedance standard substrate (ISS), i.e. the reference planes are brought to the GSG tips of the two probes. Consequently, the collected S-parameters include the behaviour of the intrinsic variable capacitor (i.e. the MEMS suspended plate) as well as the contribution due to the input/output access CPWs (see Fig. 3) plus parasitic effects, i.e. no de-embedding has been performed. Given these assumptions, we have exploited a well-known technique, usually adopted in microwave transistor modelling (Dambrine et al., 1988) based on the extraction of lumped parasitic elements that are wrapped around the intrinsic device. Fig. 4 shows the schematic of the intrinsic MEMS variable capacitor impedance and of the wrapping lumped element network accounting for the surrounding parasitic effects.

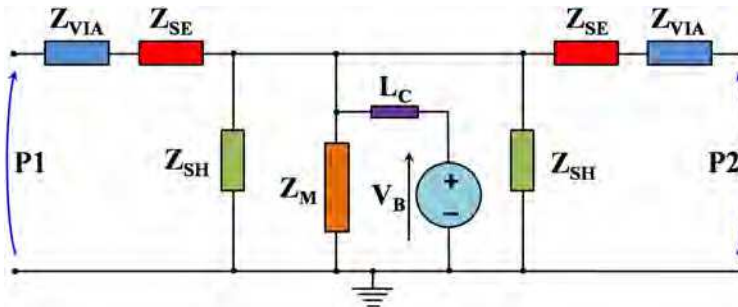


Fig. 4. Schematic of the lumped element network describing the RF behaviour of the device reported in Fig. 3. The network includes the intrinsic MEMS device and the parasitic effects.

The intrinsic MEMS impedance is indicated with  $Z_M$ , while  $Z_{SE}$  and  $Z_{SH}$  model the impedance of the access CPWs at the ports **P1** and **P2**. Furthermore,  $Z_{VIA}$  models the impedance due to the parasitic effects introduced by the gold to multi-metal through vias (explained in details later) while  $L_C$  is a choke inductor (1 mH) necessary in the Spectre simulations to decouple the DC bias from the RF signal. The lumped elements composing  $Z_M$ ,  $Z_{SE}$ ,  $Z_{SH}$  and  $Z_{VIA}$  are shown in Fig. 5.

The intrinsic MEMS variable capacitor is modelled as a shunt to ground capacitance ( $C_{MEMS}$ ), in parallel with a resistor accounting for small dielectric losses ( $R_{MEMS}$ ) and in series with an inductance ( $L_{MEMS}$ ) accounting for the contribution of the four flexible beam

suspensions (reported in Fig. 5-a). The accessing CPWs are modelled according to a well-known lumped network scheme (Pozar, 2004) shown in Fig. 5-b. It relies on a series RL section, accounting for the resistive losses within the metal and the line inductance respectively, and a parallel RC shunt section to ground, modelling the losses within the substrate and the capacitive coupling between the signal and ground planes through the air and the substrate.

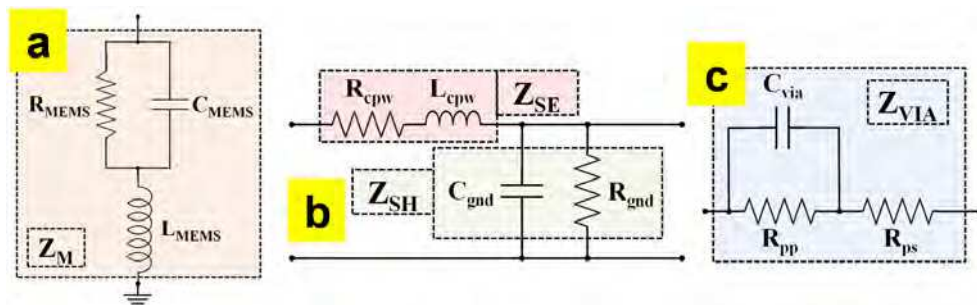


Fig. 5. Sub-networks composing the lumped element network of Fig. 4. a) Intrinsic MEMS variable capacitor; b) Input/output CPW-like line (see Fig. 3); c) Through-oxide via model accounting for the technology non-idealities.

Finally, the network of Fig. 5-c accounts for the parasitic effects due to a technology issue linked to the opening of vias through the oxide. Because of an inappropriate time end-point of the dry etching recipe performed on the batch, a very thin titanium oxide layer lays on the vias deteriorating the quality of the metal-to-metal transition (Iannacci et al., 2009, a). Such unwanted layer introduces additional losses and a series parasitic large capacitance that mainly affects the RF behaviour of the variable capacitor in the low-frequency range (as it will be discussed later in this section). Looking at Fig. 5-c, this non-ideality is modelled with a capacitance ( $C_{\text{via}}$ ) in parallel with a resistor ( $R_{\text{pp}}$ ), that models the losses in the low frequency range, plus a series resistance ( $R_{\text{ps}}$ ) accounting for the losses through the whole frequency span. Once the whole topology of the lumped element network is fixed, the specific values of all its components are tuned by using the optimization software tool available within the Agilent ADS™ framework (Iannacci et al., 2007). Suitable targets aiming at the reduction of the difference between measured and modelled S-parameters are defined. The first optimization run is performed with the S-parameters measured at 0 V bias. The optimized value of the intrinsic MEMS variable capacitor is compared with the analytical one to verify the consistency of the optimizer output. Other optimization runs are performed replacing the target of the first run with the S-parameters measured at applied voltage of 1.25 V, 2.5 V, 3.75 V and so on up to 25 V, i.e. beyond the pull-in voltage of the DUT of Fig. 3 that is around 15 V (see next subsection). The consistency of the extracted lumped element values is monitored step by step. To do this, the extracted intrinsic MEMS capacitance is cross-checked with the analytical value, computed for each voltage, from the vertical displacement known after the experimental measurements (see next subsection). All the element values of the network in Fig. 4, excluded  $C_{\text{MEMS}}$  and  $R_{\text{MEMS}}$ , do not show any significant change with the applied voltage. Once all the lumped element values are determined, they are kept fixed and only  $C_{\text{MEMS}}$  and  $R_{\text{MEMS}}$  are allowed to change. The

extracted values for all the fixed elements composing the network of Fig. 4-5 are reported in Table 1.

Input/output CPW				Via parasitic effects			MEMS
$R_{cpw}$	$L_{cpw}$	$C_{gnd}$	$R_{gnd}$	$C_{via}$	$R_{pp}$	$R_{ps}$	$L_{MEMS}$
100 m $\Omega$	122 pH	30 fF	840 G $\Omega$	134 pF	2.82 $\Omega$	700 m $\Omega$	15 pH

Table 1. Extracted value of the fixed lumped elements composing the sub-networks of Fig. 5.

The four elements composing the CPW short lines show typical values for such a structure realized in a highly conductive metal onto a high-resistivity silicon substrate, as in the case of the DUT. Differently, the parasitic effects introduced by the non-ideal through-oxide vias are rather significant, being the resistive loss quite large (700 m $\Omega$  and 2.82  $\Omega$ ) as well as the  $C_{via}$  (134 pF). Finally, the series inductance  $L_{MEMS}$  included in the intrinsic RF-MEMS device sub-network (see Fig. 5-a) is 15 pH. The two missing lumped elements in Table 1 are  $C_{MEMS}$  and  $R_{MEMS}$  as they change depending on the controlling DC voltage applied to the MEMS device. Table 2 reports their extracted values for a few applied voltages in the RF-MEMS varactor not actuated state (minimum capacitance), while Table 3 reports six cases in which the varactor is actuated (maximum capacitance).

$V_B = 0$ V		$V_B = 3.75$ V		$V_B = 10$ V		$V_B = 11.25$ V	
$R_{MEMS}$	$C_{MEMS}$	$R_{MEMS}$	$C_{MEMS}$	$R_{MEMS}$	$C_{MEMS}$	$R_{MEMS}$	$C_{MEMS}$
645 G $\Omega$	160 fF	956 G $\Omega$	185 fF	44.5 G $\Omega$	190 fF	111 G $\Omega$	192 fF

Table 2. Extracted  $R_{MEMS}$  and  $C_{MEMS}$  values (see Fig. 5-a) for different applied bias levels in the varactor not actuated state (low capacitance).

$V_B = 25$ V		$V_B = 22.5$ V		$V_B = 20$ V	
$R_{MEMS}$	$C_{MEMS}$	$R_{MEMS}$	$C_{MEMS}$	$R_{MEMS}$	$C_{MEMS}$
269 G $\Omega$	862 fF	228 G $\Omega$	804 fF	91 G $\Omega$	755 fF
$V_B = 17.5$ V		$V_B = 15$ V		$V_B = 12.5$ V	
$R_{MEMS}$	$C_{MEMS}$	$R_{MEMS}$	$C_{MEMS}$	$R_{MEMS}$	$C_{MEMS}$
276 G $\Omega$	683 fF	268 G $\Omega$	636 fF	277 G $\Omega$	551 fF

Table 3. Extracted  $R_{MEMS}$  and  $C_{MEMS}$  values (see Fig. 5-a) for different applied bias levels in the varactor actuated state (high capacitance).

Concerning the  $C_{MEMS}$  extracted values in the MEMS not actuated state there is a good agreement with the analytical ones. Indeed, by applying the well-known formula for a parallel plate capacitor, where the area of the DUT is 220x220  $\mu\text{m}^2$  and the distance between the electrodes is about 2.7  $\mu\text{m}$  (see next subsection), the capacitance value is  $\sim$ 160 fF as extracted with the method here discussed. Focusing now on the  $C_{MEMS}$  extracted in the actuated state (Table 3) it has to be highlighted that the maximum capacitance is always rather low compared to the nominal one. Indeed, when the MEMS suspended plate collapses onto the substrate there is a  $\sim$ 400 nm thick oxide layer between it and the underlying electrode, leading to a maximum capacitance of about 4 pF. However, the

extracted values show a  $C_{MAX}$  about 5 times smaller (862 fF) than the ideal one. Such reduction is mainly caused by two factors, namely, the surfaces roughness and the residual stress within the suspended gold (Iannacci et al., 2009, b). The roughness of the surfaces coming into contact (in this case the gold plate and the underneath oxide) lead to the presence of air between the two faces also when the switch is actuated. This causes the  $C_{MAX}$  to reduce as it is not anymore determined by the oxide layer only, but is given by the contribution of two series capacitors, one due to the oxide layer and the second one due to the residual air layer. Moreover, the mechanical stress that accumulates within the suspended gold during the release step (performed in plasma oxygen), usually is not uniform along the vertical dimension (stress gradient). This causes the central plate of Fig. 3 to be not perfectly planar but rather arched, thus leading to a further reduction of the contact surface and, consequently, of the  $C_{MAX}$ . The two just mentioned non-idealities are accounted for by including in the simulations and analytical calculations a constant equivalent air gap as Fig. 6 shows schematically.

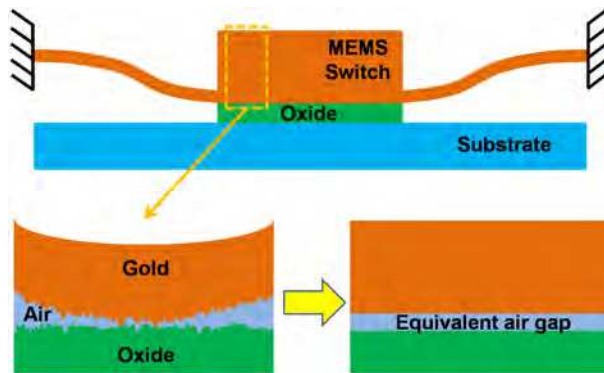


Fig. 6. *Top image*: Schematic cross-section of the actuated RF-MEMS varactor (see Fig. 3). *Bottom-left image*: Close up of one part of the actuated switch highlighting the surface roughness and the gold bowing induced by the stress gradient (both the effects are exaggerated). *Bottom-right image*: Equivalent air gap included in the simulations accounting for the just mentioned non-idealities.

After inverting the formula for the oxide and air series capacitances and using the  $C_{MAX}$  extracted value with a biasing level of 15 V (see Table 3), close to the plate release (pull-out), an equivalent air gap of 590 nm is extracted. The correctness of such value will be proven in the next subsection by means of electromechanical simulations. A final consideration has to be considered concerning the  $R_{MEMS}$ , reported in Tables 2 and 3, that in all the studied cases shows a very large value, that indicates negligible resistive losses of the intrinsic RF-MEMS varactor. Given this assumption, the  $R_{MEMS}$  can be fixed to a certain value (e.g. 100 G $\Omega$ ) in all the cases reported in Table 2 and 3 without any accuracy loss of the proposed network.

The network of Fig. 4 has been simulated within ADS with the extracted values reported in Tables 2 and 3, and the results are compared to the S-parameter measurements. The simulated and measured S11 and S21 parameters (reflection and transmission, respectively) are reported for an applied controlling voltage of 3.75 V (varactor not actuated) in Fig. 7 and for an applied bias of 25 V (varactor actuated) in Fig. 8, where the good superposition of the

curves is clearly visible. Concerning the not actuated state (Fig. 7), the influence of the parasitic effects introduced by the through-oxide vias affects both the S11 and S21 parameters up to about 2 GHz, where the reflection presents a minimum around 1 GHz, while it should be monotone, and the transmission increases with the frequency. This behaviour confirms the presence of a large unwanted series capacitance on the RF signal path acting as a spurious DC signals block. On the other hand, in the actuated state (Fig. 8) the isolation (S21) is never better than about 7 dB due to the small value of  $C_{MAX}$  compared to the nominal one and caused by the technology non-idealities already discussed. All the assumptions made up to now in the RF modelling are going to be verified by means of the electromechanical modelling.

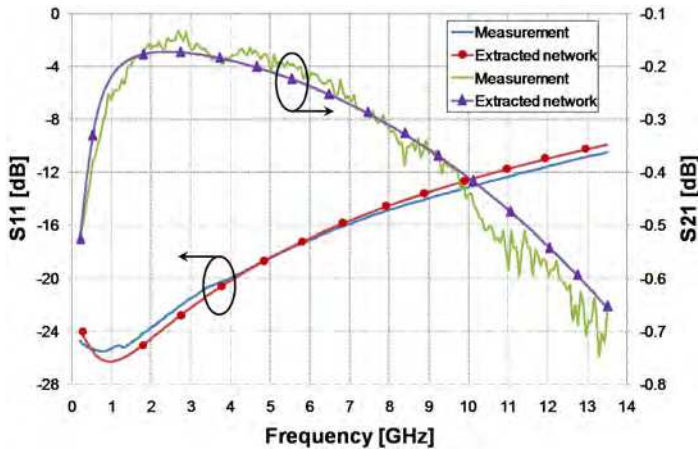


Fig. 7. Comparison of the measured and extracted (see Fig. 4) S11 and S21 parameter in the MEMS varactor not actuated state.

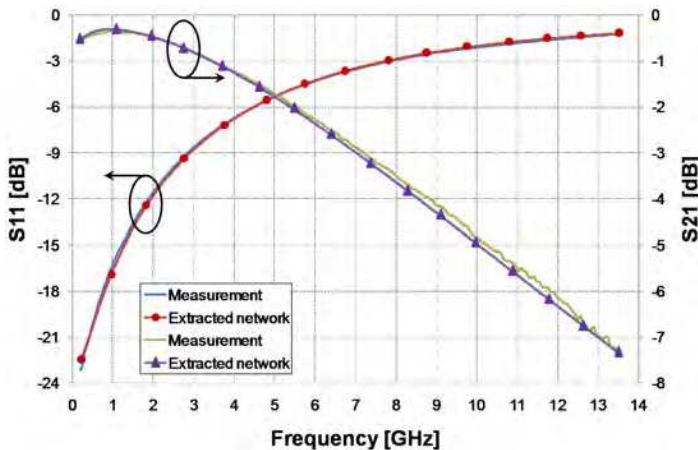


Fig. 8. Comparison of the measured and extracted (see Fig. 4) S11 and S21 parameter in the MEMS varactor actuated state.

### 3.2 Electromechanical Modelling and Verification

The electromechanical properties of the RF-MEMS varactor discussed up to now are observed once again, starting from experimental data, on the basis of which simulations are tuned and effective values accounting for the non-idealities are extracted. Verification and validation of the method discussed in previous subsection, concerning the RF domain, are reached, as the effective values extracted from electromechanical simulations coincide with the same values adopted in the RF simulations.

Fig. 9-top shows the Spectre schematic of the RF-MEMS varactor composed with the elementary MEMS models previously discussed in Section 2 for the simulation within Cadence. The central plate symbol is wired to four straight beams anchored at the opposite ends. The suspended plate is biased by means of a voltage source available within a Cadence library of standard components. Moreover, looking at Fig. 9-bottom, it is easy to identify the correspondence between the real MEMS device topology and the Spectre schematic.

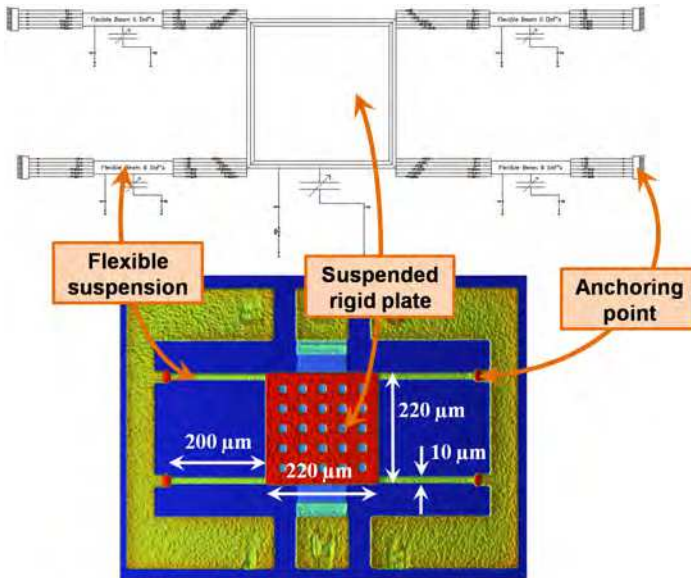


Fig. 9. Spectre schematic (top image) of the RF-MEMS varactor discussed here and assembled with the elementary components available in the software library discussed in Section 2. The correspondence between the schematic and the real device, reported in the top view measured with an optical profilometer (bottom image), is straightforward.

The RF-MEMS varactor sample of Fig. 3 and Fig. 9-bottom is measured in static regime by means of the afore-mentioned optical profilometer. A triangular symmetric voltage ranging from -20 V up to 20 V (zero mean value) with a frequency of 20 Hz is applied to the DUT. By changing the phase of the stroboscopic illuminator with respect to the biasing signal, it is possible to observe the vertical displacement of the DUT for different bias levels (Novak et al., 2003). This enables the acquisition of the whole experimental pull-in/pull-out characteristic. Subsequently, the schematic of Fig. 9-top is simulated within Spectre (DC

simulation) in order to obtain the same pull-in/pull-out characteristic. A residual air gap of 590 nm is set in the simulation when the plate collapses onto the substrate. Such value comes from the extracted  $C_{MAX}$  discussed in previous subsection. Fig. 10 reports the measured and simulated pull-in/pull-out characteristic of the RF-MEMS varactor, showing a very good agreement of the two curves. In particular, the measured pull-in voltage ( $\sim 15$  V) and pull-out voltage ( $\sim 9$  V) are predicted very accurately by the compact models in Spectre. The characteristics of Fig. 10 show the typical hysteresis of MEMS devices.

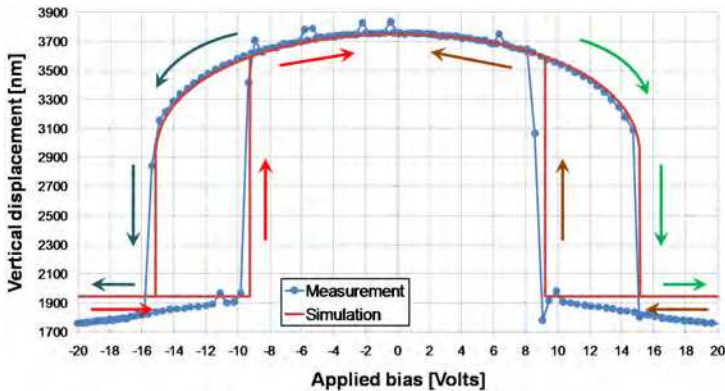


Fig. 10. Measured static pull-in/pull-out characteristic compared to the one simulated with the schematic of Fig. 9-top within Cadence (DC simulation in Spectre). Arrows help in identifying the pull-in/pull-out hysteresis.

More in details, the good agreement of the measured and simulated pull-in voltage confirms both that the elastic constant  $k$  is modelled correctly in the Spectre simulation, and that the initial air gap  $g$  is properly set (Iannacci, 2007). After this consideration, the good superposition of the measured and simulated pull-out voltage ( $V_{PO}$ ) finally confirms that the residual air gap  $t_{air}$ , previously extracted from RF measurement, is correct since the  $V_{PO}$  depends on it as follows (Iannacci et al., 2009, b):

$$V_{PO} = \sqrt{\frac{2kg(t_{ox} + t_{air})(t_{air}\epsilon_{ox} + t_{ox}\epsilon_{air})}{A\epsilon_{ox}\epsilon_{air}}} \quad (5)$$

where  $t_{air}$  is the oxide layer thickness,  $A$  the electrodes area,  $\epsilon_{ox}$  and  $\epsilon_{air}$  the dielectric constant of the oxide and air, respectively. A further confirmation of the DUT non-idealities comes from the observation of Fig. 10. Starting from the pull-in voltage ( $\sim 15$  V) and rising up to 20 V, the vertical quote of the switch is not constant as it would be expected, but tends to decrease of about 200 nm. Interpretation of such an awkward behaviour is straightforward, by knowing that the profiling system determines each point of the pull-in/pull-out characteristic as the mean value of all the vertical quotes measured onto the plate surface. Because of the plate non-planarity schematically shown in Fig. 6, after the plate pulls-in, it tends to get more flat onto the underneath oxide as a result of the attractive force increase

due to the applied voltage rise. This also explains why the extracted  $C_{MAX}$  values reported in Table 3 are larger for higher applied bias levels.

In conclusion, a few more considerations are necessary to extend the applicability of the method discussed in previous pages. In the particular case discussed in this section, the electromechanical and electromagnetic simulation of the DUT was based upon an on-purpose software tool developed by the author (Iannacci et al., 2005). However, the same method that accounts for the RF-MEMS devices non-idealities here discussed, can be effectively exploited by relying on the use of commercial simulation tools (e.g. FEM-based electromechanical and electromagnetic tools like Ansys<sup>TM</sup>, Coventor<sup>TM</sup>, Ansoft HFSS<sup>TM</sup> and so on) as well as by simply performing analytical calculations, based on the constitutive equations describing the multi-physical behaviour of RF-MEMS. The benefits of the modelling method here discussed, when dealing with the RF-MEMS design optimization, are straightforward. First of all, in the early design stage, the designer has to deal with a large number of DOFs influencing the electromechanical and electromagnetic performances, hence leading to the identifications of several trade-offs. Availability of a fast analysis method, like the just presented one, enables the designer to quickly identify the main trends linked to the variation of the available DOFs, as well as the parameters that exhibit the most significant influence on the overall RF-MEMS device/network performances. Moreover, starting from the availability of a few experimental datasets, the discussed analysis can be tailored to the effective parameters accounting for the non-idealities of the chosen technology, rather than the nominal ones. This means that the use of FEM tools, typically very accurate but time consuming, can be reserved to the final design stage, when the fine optima are sought, while the rough optimum design can be easily and quickly addressed by following the method discussed in this chapter. Since the presented procedure can be implemented and parameterized with small effort within any software tool for mathematical calculation (e.g. MATLAB<sup>TM</sup>), it is going to be synthetically reviewed and schematized as subsequent steps in the next subsection.

### 3.3 Summary of the Whole RF-MEMS Modelling Method

Starting from a lumped element description of the DUT (in this case an RF-MEMS varactor), like the one proposed in Fig. 4-5, the capacitance of the intrinsic MEMS device is known. In the case here discussed the experimental data are S-parameter measurements. However, the MEMS capacitance can also be determined by means of C-V (Capacitance vs. Voltage) measurements in AC regime, by exploiting an LCR-meter. In this case the wrapping network described in Fig. 4 is not necessary, and can be drastically simplified, as at low-frequency most of the lumped components there included are negligible. First of all, starting from the measured/extracted minimum capacitance  $C_{MIN}$  corresponding to a 0 V applied bias, the effective air gap  $g_1$  can be extracted by inverting the well-known parallel plate capacitor formula, and the oxide capacitance can be considered negligible:

$$g_1 = \frac{\epsilon_{air} A}{C_{MIN}} \quad (6)$$

Differently, given the maximum measured/extracted capacitance in the pulled-in state ( $C_{MAX}$ ), the effective air gap ( $t_{air1}$ ) due to the surface roughness and gold bowing can be determined by inverting the formula of the oxide plus air series capacitance:

$$t_{air1} = \frac{\epsilon_{air} A}{C_{MAX}} - \frac{\epsilon_{air}}{\epsilon_{ox}} t_{ox} \quad (7)$$

Let us now consider the cross-check of the extracted values by means of electromechanical measurements. Starting from the measured pull-in voltage  $V_{PI}$  and the maximum vertical displacement  $\Delta Z$ , that in the case of Fig. 10 is the quote difference between 0 V and  $\pm 16$  V applied bias (when the plate collapses onto the lower oxide layer), the effective elastic constant ( $k_{eff}$ ) accounting for the influence of residual stress on the flexible suspensions is:

$$k_{eff} = \frac{27}{8} \frac{V_{PI}^2 \epsilon_{air} A}{(\Delta Z + t_{ox})^3} \quad (8)$$

Also in this case the capacitance contribution of the oxide is neglected. Starting from the measured pull-out voltage  $V_{PO}$  and inverting its formula including the (8), the residual air gap  $t_{air2}$  is extracted as follows:

$$t_{air2} = -\frac{t_{ox}}{2} \left( 1 + \frac{\epsilon_{air}}{\epsilon_{ox}} \right) + \sqrt{\frac{t_{ox}^2}{4} \left( 1 - \frac{\epsilon_{air}}{\epsilon_{ox}} \right)^2 + \frac{V_{PO}^2 \epsilon_{air} A}{2k_{eff} \Delta Z}} \quad (9)$$

Final verification of the derived effective parameters is performed by comparing their value extracted from electromagnetic/AC measurements and electromechanical experimental data. In particular, it has to be verified that:

$$g_1 \cong t_{ox} + t_{air2} + \Delta Z \quad (10)$$

$$t_{air1} \cong t_{air2} \quad (11)$$

Now that the complete method has been described, next sections will be focused on the report of a few significant examples of its application to modelling problems referred to RF-MEMS devices and network.

#### 4. Mixed-Domain Simulation of a hybrid RF-MEMS/CMOS Voltage Controlled Oscillator (VCO)

One important feature of the discussed MEMS simulation tool is that it enables the analysis of blocks composed by different technologies, namely, RF-MEMS and standard CMOS, within the same Cadence schematic. To this purpose, the example reported in this section concerns the simulation of a hybrid Voltage Controlled Oscillator (VCO) (Tiebout, 2005).

The oscillator is designed in standard CMOS technology and implemented with the design-kit released by AMS<sup>®</sup> (0.35  $\mu\text{m}$  HBT BiCMOS S35 technology, website: www.austriamicrosystems.com). Whereas, the varactors of the LC-tank are implemented in MEMS technology with the compact models previously shown. The Cadence schematic of the VCO is shown in Fig. 11.

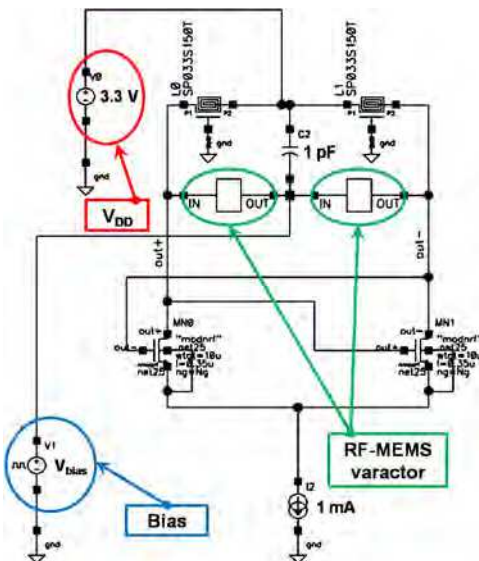


Fig. 11. Cadence schematic of the hybrid VCO composed by the CMOS oscillator in AMS technology and the RF-MEMS LC-tank.

The two symbols representing the tuneable capacitors are realized with a suspended rigid plate and four straight beams connected to its corners. Each of them corresponds to the Cadence schematic of Fig. 9-top. The two inductors within the LC-tank in Fig. 11 are also included in the design-kit provided by AMS and mentioned above. Two RF-MEMS varactors are included in the symmetric LC-tank scheme, decoupling the controlling voltage from the oscillator RF output. For the same reason, a capacitor (1 pF) is placed between the controlling voltage generator and the voltage supply ( $V_{DD} = 3.3$  V). Depending on the bias applied to the common node between the RF-MEMS varactors, their capacitance changes and consequently the oscillation frequency of the overall VCO. Transient analysis is performed in Spectre for different bias levels lower than the pull-in of the structure in Fig. 9 top (i.e. 15.6 V). The VCO tuning characteristic (frequency vs. biasing voltage) is shown in Fig. 12. The capacitance of each RF-MEMS varactor and the corresponding VCO oscillation frequency are reported in Table 4. The just shown RF-MEMS/CMOS VCO implementation represents a meaningful example about the utilization of the mixed-domain simulation environment here proposed and discussed (Iannacci, 2007).

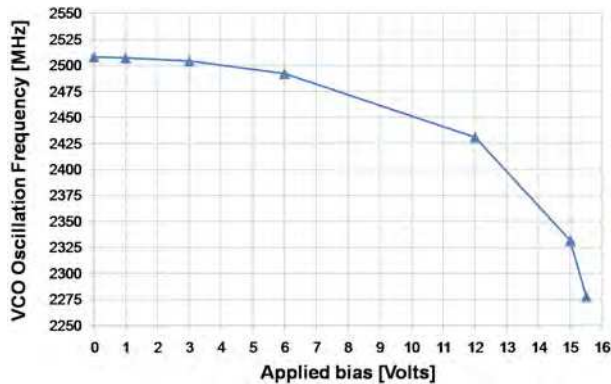


Fig. 12. VCO oscillation frequency vs. bias applied to the RF-MEMS varactors (tuning characteristic).

Bias level (V)	Capacitance (fF)	VCO Frequency (MHz)
0	597	2508
1	598	2507
3	601	2504
6	611	2492
12	671	2431
15	775	2332
15.5	838	2278

Table 4. VCO oscillation frequency depending of the bias level applied to the RF-MEMS varactors of the LC-tank.

## 5. Fast Simulation of a Reconfigurable RF-MEMS Power Attenuator

In this section the discussed MEMS compact model library is exploited in order to simulate the RF/electromechanical behaviour of a complex RF-MEMS network, namely, a multi-state reconfigurable RF/Microwave broad-band power attenuator. The network topology and performance have been already presented by the author (Iannacci et Al., 2009, a). The network is based on two resistive branches composed of 6 different resistances each, connected in series. Depending on the state (actuated/not-actuated) of 6 electrostatically controlled suspended gold membranes, it is possible to short selectively one or more resistances, thus modifying the power attenuation of the whole RF-MEMS network. Moreover, the two above mentioned branches can be selected/deselected by two SPDT (single pole double throw) stages in order to include one single resistive load or both in parallel, doubling, in turn, the number of achievable attenuation levels. A microphotograph of the whole fabricated network is reported in the top-left of Fig. 13, where the two resistive branches together with the SPDT sections are highlighted. Moreover, the top-right of Fig. 13 shows a 3D close-up of one branch composed of 6 resistances and 6 suspended membranes, and a further close-up of one single electrostatically controlled MEMS shorting switch. Both these images are obtained with an optical profiling system based on interferometry. The

bottom part of Fig. 13 reports the schematic of the whole RF-MEMS network, composed with the compact models previously discussed, within Cadence for the Spectre simulations.

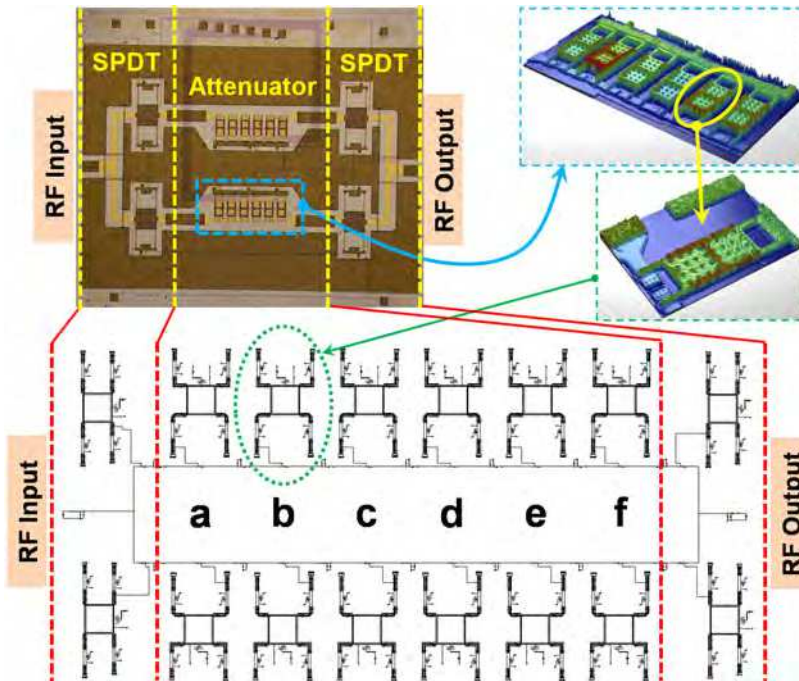


Fig. 13. Microphotograph (top-left) of the RF-MEMS reconfigurable attenuator and 3D measured profile of one of the 6 resistive loads branch and of one MEMS suspended membrane (top-right). Spectre schematic (bottom-image) of the whole network composed with the compact models discussed above. The 6 resistive loads are labelled with the letters “a,b,c,d,e,f”. The correspondence between the real network and the schematic is highlighted.

The resistance value for each of the 6 loads, as it results from measurements, is reported in Table 5 (Iannacci et Al., 2009, a). The Spectre schematic is completed with extracted lumped element sections similar to the ones of Fig. 4 and 5 (too small to be distinguished in figure), accounting for the short CPW portions included in the network layout (see Fig. 13 top-left).

a	b	c	d	e	f
9.3 $\Omega$	18.6 $\Omega$	18.6 $\Omega$	93 $\Omega$	206 $\Omega$	206 $\Omega$

Table 5. Value of the 6 resistive loads included in each branch of the reconfigurable RF-MEMS attenuator of Fig. 13.

Mixed S-parameter/electromechanical simulations are performed in Spectre on the schematic of Fig. 13. In particular, Fig. 14 refers to the RF behaviour of the network when only one of the two branches is selected. Starting from the configuration introducing the maximum attenuation (i.e. none of the 6 membranes is actuated), the MEMS suspended

membranes are actuated (pull-in) in sequence (1, 2,...6 actuated), showing that when a resistance is shorted the corresponding attenuation level decreases from DC up to 40 GHz.

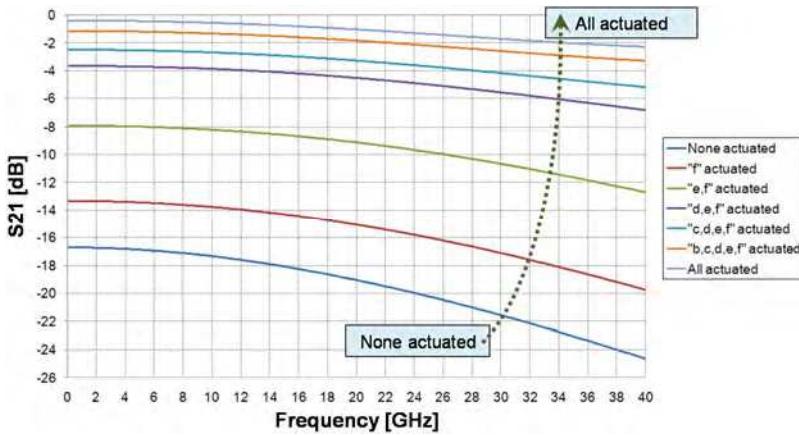


Fig. 14. S21 parameter behaviour of the RF-MEMS multi-state attenuator simulated in Spectre. When a MEMS membrane pulls-in, thus shorting the corresponding resistive load, the attenuation level decreases and the shift of the transmission parameter is proportional to the resistance value (see Table 5).

The same schematic has been simulated with both the resistive branches inserted (resistances in parallel). In this case the S-parameter simulation is performed at a single frequency (20 GHz) and the bias DC voltage, controlling each of the 6 shorting suspended membranes, is alternatively swept between 0 and 20 V. Fig. 15 shows the results highlighting the pull-in voltage of the membranes that is around 13 V.

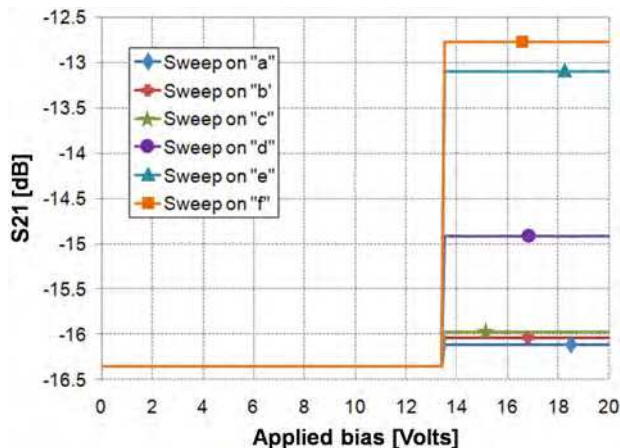


Fig. 15. S21 parameter behaviour simulated in Spectre at 20 GHz vs. the DC bias applied to the selecting suspended membranes. The attenuation shift depends on the resistance value.

The S21 parameter change depends on the value of the shorted resistive load. Moreover, it should be noted that the maximum attenuation level (i.e. none of the membranes actuated) is about 16.5 dB (as visible in Fig. 15 for applied voltage lower than the pull-in) while in Fig. 14 it is about 19 dB at 20 GHz. The reason for this difference is that the simulations reported in Fig. 15 refer to both the branches connected in parallel and, consequently, to a lower load resistance.

## 6. Lumped-Element Network of In-Package Coplanar Wave-Guide Structures

This last section is devoted to the description of the RF behaviour due to the package. Indeed, RF-MEMS devices (as well as MEMS in general) are very fragile against environmental factors (like moisture, dust particles, shocks and so on) due to their characteristics (Gilleo, 2005). Because of these motivations, RF-MEMS devices need to be encapsulated within a package that can just isolate them from the external environment, or even enhance their performance by ensuring specific working conditions. In the latter case, the vacuum condition within the packaged housing for a MEMS resonator increases dramatically its Q-Factor (Nguyen, 2004). In turn, application of a package to RF-MEMS devices introduces additional losses and impedance mismatch, due to the increased signal path and discontinuities, indeed affecting their performances. Given these considerations, the package design and fabrication has to be thought carefully in order to minimize its impact on the RF-MEMS devices/networks performance. The author already presented an approach to the electromagnetic (EM) optimization of the package layout for RF-MEMS within a given technology, based on the implementation of a parameterized 3D model within a commercial FEM-based EM tool, and validated against experimental data (Iannacci et Al., 2008). In this section, the focus is going to be concentrated on the RF simulation of the package based on lumped element networks, thus pushing forward the methodology discussed in previous pages, aiming at a complete description of RF-MEMS devices/networks. The structure to be analyzed is a standard CPW (Coplanar Wave-Guide) instead of complete RF-MEMS devices, as they are based on the CPW topology. To this purpose, a CPW has been simulated within the Ansoft HFSS™ EM tool in air at first, and then with the package model described in (Iannacci et Al., 2008). Both the CPW and package characteristics, as well as the wafer-to-wafer bonding technique, are based on the technology process available at the DIMES Research Centre (Technical University of Delft, the Netherlands) (Iannacci et Al., 2006). In particular, the package is based on vertical through wafer vias for the signal redistribution from the MEMS device wafer to the external world.

Fig. 16 shows the HFSS 3D schematic of an uncapped CPW (left-image) and of the same CPW with the package (right-image), where vertical vias and top CPW are visible (the package substrate was hidden to allow the vias view). The CPW reported in Fig. 16 has been first simulated within HFSS without any package. The silicon substrate thickness is 500  $\mu\text{m}$  and its resistivity is 2 K $\Omega\cdot\text{cm}$ . The CPW is 2 mm long, the signal line width, ground lines width and gap are 100  $\mu\text{m}$ , 700  $\mu\text{m}$  and 50  $\mu\text{m}$ , respectively. Finally, the CPW is realized in a 2  $\mu\text{m}$  thick electrodeposited copper layer. Subsequently, the CPW with package (Fig. 16-right) is simulated and, being the model parameterized, a few features, like vertical vias diameter and lateral distance between the signal and ground vias, were changed. The package is also realized with a 500  $\mu\text{m}$  thick and 2 K $\Omega\cdot\text{cm}$  silicon substrate and vertical through-wafer vias are opened with the deep reactive ion etching (DRIE) and filled

(electrodeposition) with copper. The top CPWs (see Fig. 16-right) are also made of copper. Their dimensions are the same of the uncapped CPW, apart from the length that is  $500\ \mu\text{m}$ , and have been also simulated in HFSS as standalone structures. A lumped element network describing the packaged transmission line is built and its components values are extracted with the ADS optimization tool as previously described in Subsection 3.1.

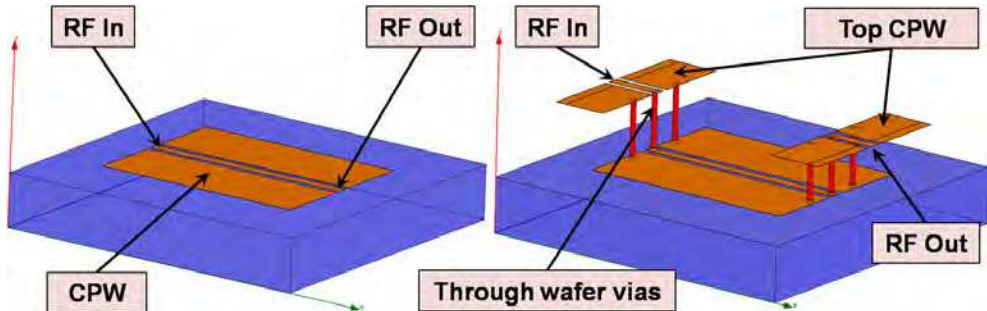


Fig. 16. HFSS schematic of an uncapped CPW (left-image) and of the same CPW with the package (right-image). The package substrate is removed to allow the view of vertical vias.

The extracted network schematic is shown in Fig. 17 where the blocks labelled as “CPW” and “Top CPW” are items available within ADS in order to link the data, simulated in HFSS and provided in Touchstone format, of the CPW of Fig. 16-left and of the top CPW (see Fig. 16-right), respectively. All the other lumped elements are placed in the schematic according to the expected behaviour of each part of the package, i.e. vertical vias, solder bumps, discontinuity between the top CPWs and vertical vias and interaction of the package with the EM field above the capped CPW.

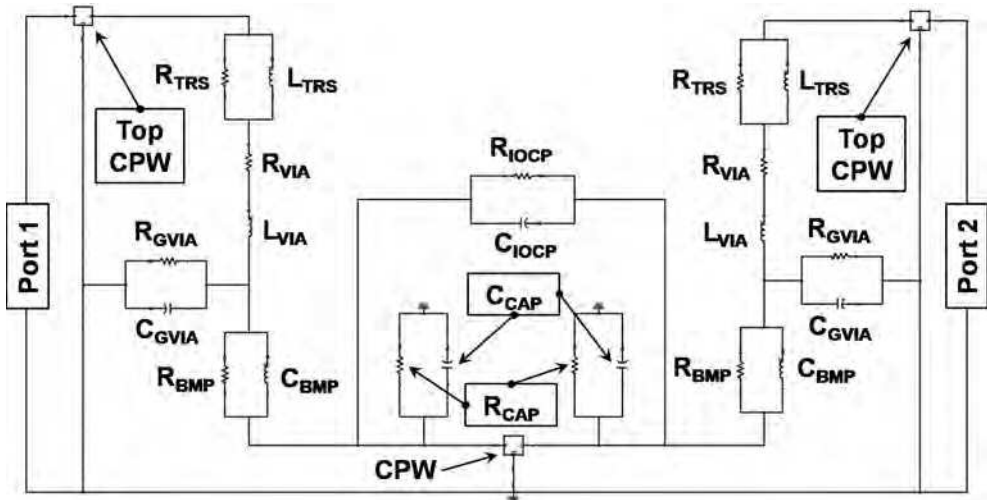


Fig. 17. Schematic of the lumped-element network describing the packaged CPW previously shown in Fig. 16-right.

The ground-signal-ground vertical vias are modelled according to the scheme of a standard CPW (Pozar, 2004) and the corresponding elements within the schematic of Fig. 17 are labelled as:  $R_{VIA}$ ,  $L_{VIA}$ ,  $R_{GVIA}$  and  $C_{GVIA}$ . The transitions between the top CPW and the vertical vias are modelled as a resistance and inductance in parallel ( $R_{TRS}$ ,  $L_{TRS}$ ) as well as the solder bumps connecting vertical vias with the capped CPW ( $R_{BMP}$ ,  $L_{BMP}$ ). Additional losses and capacitive coupling to ground, induced by the presence of the package above the CPW, are modelled with  $C_{CAP}$  and  $R_{CAP}$  and, finally, the direct input/output coupling through the cap is accounted for by  $R_{IOCP}$  and  $C_{IOCP}$ . As initial case, a package with a 500  $\mu\text{m}$  thick silicon substrate, vertical via diameter of 50  $\mu\text{m}$  and lateral pitch of 250  $\mu\text{m}$  (considered between the centre of the signal and of the ground vias) is taken into account. Starting from the HFSS simulation of such structure, the lumped elements value is extracted within ADS and reported in Table 6, thus validating the topology reported in Fig. 17 in the frequency range from 1 GHz up to 15 GHz.

$R_{VIA}$	$L_{VIA}$	$R_{GVIA}$	$C_{GVIA}$	$R_{TRS}$	$L_{TRS}$
110 m $\Omega$	148 pH	630 M $\Omega$	62.6 fF	331 m $\Omega$	41 pH
$R_{BMP}$	$L_{BMP}$	$C_{CAP}$	$R_{CAP}$	$R_{IOCP}$	$C_{IOCP}$
9.07 $\Omega$	55 pH	1 fF	200 G $\Omega$	820 G $\Omega$	17.4 fF

Table 6. Values extracted for the elements of the schematic reported in Fig. 17 for a 500  $\mu\text{m}$  thick silicon package, with vias diameter of 50  $\mu\text{m}$  and lateral pitch of 250  $\mu\text{m}$ .

Fig. 18 reports the S11 and S21 parameters comparison between HFSS simulations of the packaged CPW and the network of Fig. 17 with the value reported in Table 6, showing a very good superposition of the curves.

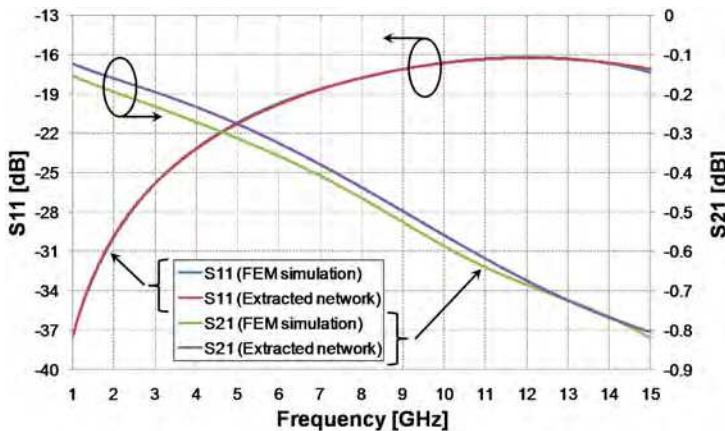


Fig. 18. Comparison of the simulated (in HFSS) and extracted network (see Fig. 17 and Table 6) S11 and S21 parameters in the frequency range from 1 GHz up to 15 GHz.

Subsequently, some critical technology degrees of freedom related to the package are alternatively modified in order to validate, on one side, the correctness of the topology reported in Fig. 17, and to analyze the influence of such variations on the network lumped

components. Starting from the lateral via pitch, the whole structure is simulated in HFSS with a value of 200  $\mu\text{m}$  and 300  $\mu\text{m}$ , respectively, smaller and larger compared to the initial case discussed above. The ADS optimization is repeated for these cases and the only parameters allowed to change are  $R_{\text{GVIA}}$  and  $C_{\text{GVIA}}$ . Their comparison concerning the three vias lateral pitch is reported in Table 7.

200 $\mu\text{m}$ vias pitch		250 $\mu\text{m}$ vias pitch		300 $\mu\text{m}$ vias pitch	
$R_{\text{GVIA}}$	990 M $\Omega$	$R_{\text{GVIA}}$	630 M $\Omega$	$R_{\text{GVIA}}$	960 M $\Omega$
$C_{\text{GVIA}}$	101 fF	$C_{\text{GVIA}}$	62.6 fF	$C_{\text{GVIA}}$	35.7 fF

Table 7. Values of the coupling capacitance and resistive loss between the signal and ground vias for different vias lateral pitches. The highlighted row corresponds to the most significant parameter exhibiting variations.

As expected, the coupling capacitance between the signal and ground vias increases when the lateral distance is smaller and decreased for a larger pitch. On the other hand, the resistive losses are so small that their variations can be neglected, as already mentioned in Subsection 3.1. However, such elements are kept in the network in order to extend its suitability to lossy substrates. Comparison of the S-parameters behaviour of the HFSS simulations and the network of Fig. 17 with the values reported in Table 7 (not reported here for sake of brevity) shows a good agreement as reported in Fig. 18. Another modified DOF is the via diameter. Starting from the capped CPW with lateral via pitch of 200  $\mu\text{m}$  and silicon substrate thickness of 500  $\mu\text{m}$ , via diameter is increased to 70  $\mu\text{m}$  and 85  $\mu\text{m}$ . In this case all the via parameters ( $R_{\text{VIA}}$ ,  $L_{\text{VIA}}$ ,  $R_{\text{GVIA}}$  and  $C_{\text{GVIA}}$ ) are allowed to change as well as the ones of the top CPW-to-via discontinuity ( $R_{\text{TRS}}$ ,  $L_{\text{TRS}}$ ) and via-to-solder bumps discontinuity ( $R_{\text{BMP}}$ ,  $L_{\text{BMP}}$ ). The extracted values are reported in Table 8.

50 $\mu\text{m}$ via diameter		70 $\mu\text{m}$ via diameter		85 $\mu\text{m}$ via diameter	
$R_{\text{VIA}}$	110 m $\Omega$	$R_{\text{VIA}}$	98 m $\Omega$	$R_{\text{VIA}}$	56 m $\Omega$
$L_{\text{VIA}}$	148 pH	$L_{\text{VIA}}$	82 pH	$L_{\text{VIA}}$	70 pH
$R_{\text{GVIA}}$	630 M $\Omega$	$R_{\text{GVIA}}$	188 G $\Omega$	$R_{\text{GVIA}}$	448 G $\Omega$
$C_{\text{GVIA}}$	62.6 fF	$C_{\text{GVIA}}$	100 fF	$C_{\text{GVIA}}$	120 fF
$R_{\text{TRS}}$	331 m $\Omega$	$R_{\text{TRS}}$	314 m $\Omega$	$R_{\text{TRS}}$	100 m $\Omega$
$L_{\text{TRS}}$	41 pH	$L_{\text{TRS}}$	10 pH	$L_{\text{TRS}}$	25 pH
$R_{\text{BMP}}$	9.07 $\Omega$	$R_{\text{BMP}}$	3.15 $\Omega$	$R_{\text{BMP}}$	2 $\Omega$
$L_{\text{BMP}}$	55 pH	$L_{\text{BMP}}$	20 pH	$L_{\text{BMP}}$	20 pH

Table 8. Values of the via parameters, top CPW-to-via and via-to-solder bumps transitions for vertical vias diameter of 50  $\mu\text{m}$ , 70  $\mu\text{m}$  and 85  $\mu\text{m}$ . The highlighted rows correspond to the most significant parameters exhibiting variations.

As final case, given the via diameter of 50  $\mu\text{m}$  and the lateral pitch of 200  $\mu\text{m}$ , the silicon package thickness is reduced to 400  $\mu\text{m}$  and 300  $\mu\text{m}$ . In this case all the via parameters ( $R_{\text{VIA}}$ ,  $L_{\text{VIA}}$ ,  $R_{\text{GVIA}}$  and  $C_{\text{GVIA}}$ ) are allowed to change as well as the additional coupling to ground and input/output elements ( $C_{\text{CAP}}$ ,  $R_{\text{CAP}}$ ,  $R_{\text{IOCP}}$  and  $C_{\text{IOCP}}$ ).

500 $\mu\text{m}$ cap thickness		400 $\mu\text{m}$ cap thickness		300 $\mu\text{m}$ cap thickness	
$R_{\text{VIA}}$	110 m $\Omega$	$R_{\text{VIA}}$	62 m $\Omega$	$R_{\text{VIA}}$	20 m $\Omega$
$L_{\text{VIA}}$	148 pH	$L_{\text{VIA}}$	54 pH	$L_{\text{VIA}}$	51 pH
$R_{\text{GVIA}}$	990 M $\Omega$	$R_{\text{GVIA}}$	5 G $\Omega$	$R_{\text{GVIA}}$	4.8 G $\Omega$
$C_{\text{GVIA}}$	101 fF	$C_{\text{GVIA}}$	52 fF	$C_{\text{GVIA}}$	41 fF
$C_{\text{CAP}}$	1 fF	$C_{\text{CAP}}$	15 fF	$C_{\text{CAP}}$	1 fF
$R_{\text{CAP}}$	200 G $\Omega$	$R_{\text{CAP}}$	225 G $\Omega$	$R_{\text{CAP}}$	204 G $\Omega$
$R_{\text{IOCP}}$	820 G $\Omega$	$R_{\text{IOCP}}$	912 G $\Omega$	$R_{\text{IOCP}}$	828 G $\Omega$
$C_{\text{IOCP}}$	17.4 fF	$C_{\text{IOCP}}$	2.3 fF	$C_{\text{IOCP}}$	1 fF

Table 9. Values of the via parameters and additional coupling/loss due to the cap for a package thickness of 500  $\mu\text{m}$ , 400  $\mu\text{m}$  and 300  $\mu\text{m}$ . The highlighted rows correspond to the most significant parameters exhibiting variations.

In conclusion, despite a few elements included in the network of Fig. 17 do not show significant changes, the most critical parameters (highlighted in Tables 7-9) change in compliance with physical consideration related to the package geometry variations in the FEM analyses. For example, the vias shunt (to ground) coupling capacitance decreases as the vias lateral pitch increases as well as when the cap thickness lowers. This proves the suitability of the chosen network (Fig. 17). Following the same approach, similar network topologies can be extracted referring to other frequency ranges, depending on the specific application the designer aims at.

## 7. Conclusion

In this chapter several aspects related to the mixed-domain electromechanical and electromagnetic simulation of RF-MEMS devices and network were reported. First of all, a fast simulation tool based on a lumped components MEMS model software library, previously developed by the author, was introduced and discussed. The elementary components, implemented in VerilogA programming language, within the Cadence IC development environment, are the flexible straight beam and the rigid suspended plate electromechanical transducer. Such elements, suitably connected together, allow the composition of complete RF-MEMS topologies and their fast simulation by means of the Spectre simulator.

Subsequently, the exploitation of the just mentioned software tool was discussed referring to an RF-MEMS variable capacitor (varactor), manufactured in the FBK surface micromachining technology. In particular, the model library was used in order to model the electromechanical behaviour (static pull-in/pull-out) of the mentioned varactor, also accounting for the most critical technology non-idealities, namely, residual stress within the electrodeposited gold and the surface roughness.

A methodology has been then discussed in details concerning the RF modelling of the variable capacitor. It is based on the extraction of a lumped-element network, accounting for the behaviour of the intrinsic device (shunt-to-ground tuneable capacitance), plus all the parasitic effects surrounding it, e.g. inductance, losses and coupling due to the input/output short CPW sections. Once the network arrangement is set, values of the lumped components are extracted

by means of a commercial optimization tool, aiming at reproducing the S-parameters experimental characteristic of the tested device. The appropriateness of the defined network is validated both targeting several measured datasets, where only the intrinsic capacitance changes (collected for different applied bias levels), and comparing the corrective factors needed to account for the non-idealities in the electromechanical and electromagnetic modelling stages.

Furthermore, the fast simulation tool use was demonstrated also in the analysis of a hybrid RF-MEMS/CMOS voltage controlled oscillator (VCO).

Subsequently, the lumped element network approach was exploited also to simulate a complex RF-MEMS network, i.e. a reconfigurable RF/Microwave power attenuator, composed by multi-state resistive branches. In order to complete the overview on possible applications of the discussed modelling methodology, a lumped element network was extracted for a packaged CPW, based on FEM simulations of such structure (with and without cap).

By following the sequence suggested in this chapter, it is possible, stage after stage, to model all the critical aspects influencing the RF behaviour of the MEMS-based structures to be analyzed, like parasitic effects due to the device itself as well as introduced by the package, thus leading to a complete and accurate description of the real device that enables, at the same time, very fast simulations.

Application of such an approach eases the design phase that could be significantly speeded up by the definition of parameterized models, accounting for the parasitic effects plus package within a given technology. The just mentioned parametric models can be straightforwardly set up with the notions presented in this chapter. Moreover, the availability of the MEMS software library, developed by the author, would help in pursuing a complete, fast and accurate preliminary design of new MEMS-based RF simple component or networks. However, the method can be exploited even without such tool, as the main formulae describing the electromechanical behaviour of MEMS devices, as well as the non-idealities arising from the specific adopted technology process, were shown in details.

In conclusion, the material presented and discussed in this chapter might be of significant help for those who are involved in the design and performance optimization of RF-MEMS devices and networks. Indeed, the proposed methodology allows the inclusion of significant aspects of real devices, like technology non-idealities and RF parasitic effects, by keeping the simulation time and complexity very low.

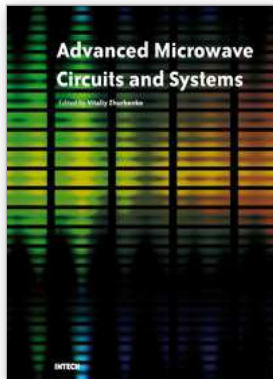
Such method is very effective in the initial design optimization, when several degrees of freedom have to be studied, highlighting the trade-offs linking them. However, the method cannot completely replace the use of more accurate FEM tools, but can, in turn, reserve their use to the final optima definition, thus optimizing the time necessary to reach the desired final design, starting from a rough idea about the initial topology that could better suit the application requirements.

## 8. References

- Chung, D.J.; Anagnostou, D.; Ponchak, G. & Tentzeris, M.M.; Papapolymerou, J. (2007). Light Weight MIMO Phased Arrays with Beam Steering Capabilities using RF MEMS, *Proceedings of the IEEE 18th International Symposium on Personal, Indoor and Mobile Radio Communications, PIMRC 2007*, pp. 1-3, ISBN 978-1-4244-1144-3, Athens, Greece, Sep. 2007, IEEE

- Dambrine, G.; Cappy, A.; Heliodore, F. & Playez, E. (1988). A new method for determining the FET small-signal equivalent circuit. *IEEE Transactions on Microwave Theory and Techniques*, Vol. 36, No. 7, (Jul. 1988) page numbers (1151-1159), ISSN 0018-9480
- Daneshmand, M. & Mansour, R. R. (2007). Redundancy RF MEMS Multi-Port Switches and Switch Matrices. *IEEE/ASME Journal of Microelectromechanical Systems*, Vol. 16, No. 2, (Apr. 2007) page numbers (296-303), ISSN 1057-7157
- De Los Santos, H. J. (2002). *RF MemS Circuit Design for Wireless Communications*, Artech House, ISBN 1-58053-329-9, Boston, USA
- Ettxeberria, J.A. & Gracia, F.J. (2007). High Q factor RF MEMS Tunable Metallic Parallel Plate Capacitor, *Proceedings of the Spanish Conference on Electron Devices, 2007*, pp. 201-204, ISBN 1-4244-0868-7, Madrid, Spain, Jan. 2007, Piscataway, NJ
- Fedder, G. (2003). Issues in MEMS macromodeling, *Proceedings of the 2003 IEEE/ACM Int. Workshop on Behavioral Modeling and Simulation (BMAS '03)*, pp. 64-69, ISBN 0-780-38135-1, San Jose, CA, USA, Oct. 2003, IEEE
- Gilleo, K. (2005). *MEMS/MOEM Packaging*, McGraw-Hill, ISBN 0-071-45556-6, Hoboken, NJ
- Goldsmith, C.L.; Zhimin Yao; Eshelman, S. & Denniston, D. (1998). Performance of low-loss RF MEMS capacitive switches. *Microwave and Guided Wave Letters*, Vol. 8, No. 8, (Aug. 1998) page numbers (269-271), ISSN 1051-8207
- Hyung, S.L.; Young, J. Y.; Dong-Hoon, C. & Jun-Bo, Y. (2008). High-Q, tunable-gap MEMS variable capacitor actuated with an electrically floating plate, *Proceedings of the IEEE 21st International Conference on Micro Electro Mechanical Systems*, pp. 180-183, ISBN 978-1-4244-1793-3, Tucson, Arizona, USA, Jan. 2008, IEEE
- Iannacci, J.; Del Tin, L.; Gaddi, R.; Gnudi, A. & Rangra, K. J. (2005). Compact modeling of a MEMS toggle-switch based on modified nodal analysis, *Proceedings of the Symposium on Design, Test, Integration and Packaging of MEMS/MOEMS (DTIP 2005)*, pp. 411-416, ISBN 2-84813-0357-1, Montreux, Switzerland, Jun. 2005
- Iannacci, J.; Bartek, M.; Tian, J. & Sosin, S. (2006). Hybrid Wafer-Level Packaging for RF MEMS Applications, *Proceedings of the 39th International Symposium on Microelectronics (IMAPS 2006)*, pp. 246-253, ISBN 0-930815-80-7, San Diego, CA, USA, Oct. 2006, IMAPS, Washington, DC, USA
- Iannacci, J. (2007). *Mixed Domain Simulation and Hybrid Wafer Level Packaging of RF MEMS Devices for Wireless Applications*, Ph.D. Thesis Dissertation, University of Bologna, Italy, March 2007, ISBN, Available at: <http://amsdottorato.cib.unibo.it/464/>
- Iannacci, J.; Gaddi, R. & Gnudi, A. (2007). Non-Linear Electromechanical RF Model of a MEMS Varactor Based on VerilogA<sup>®</sup> and Lumped Element Parasitic Network, *Proceedings of the 37th European Microwave Conference (EuMC)*, pp. 544-547, ISBN 978-2-87487-000-2, Munich, Germany, Oct. 2007, Horizon House Publications Ltd, London, UK
- Iannacci, J.; Bartek, M.; Tian, J.; Gaddi, R. & Gnudi, A. (2008). Electromagnetic Optimisation of an RF-MEMS Wafer-Level Package. *Sensors and Actuators A: Physical, Special Issue of Eurosensors XX 2006 Conference*, Vol. 142, No. 1, (Mar. 2008) page numbers (434-441), ISSN 0924-4247
- Iannacci, J.; Giacomozzi, F.; Colpo, S.; Margesin, B. & Bartek, M. (2009). A General Purpose Reconfigurable MEMS-Based Attenuator for Radio Frequency and Microwave Applications, *Proceedings of the IEEE Region 8 EUROCON 2009 Conference*, pp. 1201-1209, ISBN 978-1-4244-3861-7, Saint Petersburg, Russia, May 2009, IEEE

- Iannacci, J.; Repchankova, A.; Macii, D. & Niessner, M. (2009). A Measurement Procedure of Technology-related Model Parameters for Enhanced RF-MEMS Design, *Proceedings of the IEEE International Workshop on Advanced Methods for Uncertainty Estimation in Measurement AMUEM 2009*, pp. 44-49, ISBN 978-1-4244-3593-7, Bucharest, Romania, Jul. 2009, IEEE
- Jing, Q.; Mukherjee, T. & Fedder, G. (2002). Schematic-Based Lumped Parameterized Behavioral Modeling for Suspended MEMS, *Proceedings of the ACM/IEEE International Conference on Computer Aided Design (ICCAD '02)*, pp. 367-373, ISBN 0-7803-7607-2, San Jose, CA, USA, Nov. 2002, ACM, New York, NY, USA
- Larcher, L.; Brama, R.; Ganzerli, M.; Iannacci, J.; Margesin, B.; Bedani, M. & Gnudi, A. (2009). A MEMS Reconfigurable Quad-Band Class-E Power Amplifier for GSM Standard, *Proceedings of the 22nd IEEE International Conference on Micro Electro Mechanical Systems MEMS 2009*, pp. 864-867, ISBN 978-1-4244-2978-3, Sorrento, Italy, Jan. 2009, IEEE, Piscataway, NJ, USA
- Maciel, J.J.; Slocum, J.F.; Smith, J.K. & Turtle, J. (2007). MEMS Electronically Steerable Antennas for Fire Control Radars, *Proceedings of the IEEE Radar Conference 2007*, pp. 677-682, ISBN 1-4244-0284-0, Boston, MA, USA, Apr. 2007, IEEE
- Nguyen, C.T.-C. (2004). Vibrating RF MEMS for next generation wireless applications, *Proceedings of the IEEE Custom Integrated Circuits Conference*, pp. 257-264, ISBN 0-7803-8495-4, Orlando, FL, USA, Oct. 2004, IEEE
- Novak, E.; Wan, D. S.; Unruh, P. & Schurig, M. (2003). MEMS Metrology Using a Strobed Interferometric System, *Proceedings of the XVII IMEKO World Congress*, pp. 178-182, ISBN 953-7124-00-2, Dubrovnik, Croatia, Jun. 2003, Kluwer Academic Publisher, Norwell, MA
- Pozar, D. M. (2004). *Microwave Engineering*, J. Wiley & S., ISBN 0-471-44878-8, Hoboken, NJ
- Przemieniecki, J. S. (1968). *Theory of Matrix Structural Analysis*, McGraw-Hill, ISBN 0-486-64948-2, New York, NJ
- Rebeiz, G.M. & Muldavin, J.B. (2001). RF MEMS switches and switch circuits. *IEEE Microwave Magazine*, Vol. 2, No. 4, (December 2001) page numbers (59-71), ISSN 1527-3342
- Tiebout, M. (2005). *Low Power Vco Design in CMOS*, Springer Technology & Industrial Arts, ISBN 3-540-24324-0, New York, NJ
- Topalli, K.; Aydin Civi, O.; Demir, S.; Koc, S. & Akin, T. (2008). A Monolithic Phased Array using 3-bit DMTL RF MEMS Phase Shifters. *IEEE Transactions on Microwave Theory and Techniques*, Vol. 56, No. 2, (Feb. 2008) page numbers (270-277), ISSN 0018-926X
- Varadan, V. K. (2003). *RF MemS & Their Applications*, John Wiley & Sons, ISBN 0-470-84308-X, Hoboken, NJ
- Zine-El-Abidine, I.; Okoniewski, M. & McRory, J.G. (2003). A new class of tunable RF MEMS inductors, *Proceedings of the International Conference on MEMS, NANO and Smart Systems*, pp. 114-115, ISBN 0-7695-1947-4, Banff, Alberta, Canada, Jul. 2003, IEEE



## **Advanced Microwave Circuits and Systems**

Edited by Vitaliy Zhurbenko

ISBN 978-953-307-087-2

Hard cover, 490 pages

**Publisher** InTech

**Published online** 01, April, 2010

**Published in print edition** April, 2010

This book is based on recent research work conducted by the authors dealing with the design and development of active and passive microwave components, integrated circuits and systems. It is divided into seven parts. In the first part comprising the first two chapters, alternative concepts and equations for multiport network analysis and characterization are provided. A thru-only de-embedding technique for accurate on-wafer characterization is introduced. The second part of the book corresponds to the analysis and design of ultra-wideband low-noise amplifiers (LNA).

### **How to reference**

In order to correctly reference this scholarly work, feel free to copy and paste the following:

Jacopo Iannacci (2010). Mixed-Domain Fast Simulation of RF and Microwave MEMS-based Complex Networks within Standard IC Development Frameworks, *Advanced Microwave Circuits and Systems*, Vitaliy Zhurbenko (Ed.), ISBN: 978-953-307-087-2, InTech, Available from:  
<http://www.intechopen.com/books/advanced-microwave-circuits-and-systems/mixed-domain-fast-simulation-of-rf-and-microwave-mems-based-complex-networks-within-standard-ic-deve>

# **INTECH**

open science | open minds

### **InTech Europe**

University Campus STeP Ri  
Slavka Krautzeka 83/A  
51000 Rijeka, Croatia  
Phone: +385 (51) 770 447  
Fax: +385 (51) 686 166  
[www.intechopen.com](http://www.intechopen.com)

### **InTech China**

Unit 405, Office Block, Hotel Equatorial Shanghai  
No.65, Yan An Road (West), Shanghai, 200040, China  
中国上海市延安西路65号上海国际贵都大饭店办公楼405单元  
Phone: +86-21-62489820  
Fax: +86-21-62489821

© 2010 The Author(s). Licensee IntechOpen. This chapter is distributed under the terms of the [Creative Commons Attribution-NonCommercial-ShareAlike-3.0 License](#), which permits use, distribution and reproduction for non-commercial purposes, provided the original is properly cited and derivative works building on this content are distributed under the same license.